energies

MDPI

*Article*

# CFD and Statistical Analysis of the Impact of Surface Physical Parameters on the Thermal Resistance of Layered Partitions in ETICS Systems

**Arkadiusz Urzędowski [1,*], Andrzej Sachajdak [2], Arkadiusz Syta [1] and Jacek Zaburko [1]**

[1] Faculty of Mathematics and Information Technology, Lublin University of Technology, Nadbystrzycka 38, 20-618 Lublin, Poland; a.syta@pollub.pl (A.S.)

[2] Department of Thermal Technology, Silesian University of Technology, Konarskiego 22, 44-100 Gliwice, Poland; andrzej.sachajdak@polsl.pl

* Correspondence: a.urzedowski@pollub.pl; Tel.: +48-690006777

**Abstract:** In the article, the authors attempted to analyze the impact of such materials factors as surface emissivity, surface roughness, air gap thickness, and type of concrete on heat transport in the microstructure of vertical multilayer building walls. The surface analysis conducted using three-dimensional modeling tools provided information about the formation of its microstructure before and after the application of a reflection-smoothing coating, which has a direct impact on the emissivity of the surface and was reduced from 0.93 to 0.29. Thermal analyses demonstrated that after applying the reflective coating, thermal resistance increased significantly in the air gap, by approximately 86%, which resulted in a 28% improvement of the evaluated walls samples. The studies have shown that increasing the gap thickness between concrete and thermal insulation results in a thermal resistance increase. It is feasible to enhance the thermal insulation of walls while simultaneously reducing their thickness, a development that holds significant potential for application in the production of prefabricated sandwich panels. The statistical analyzes performed showed significant differences between the analyzed configurations.

**Keywords:** heat transfer in walls; CFD; surface emissivity

check for updates

Academic Editor: Francesco Nocera

Received: 19 November 2024
Revised: 17 December 2024
Accepted: 27 December 2024
Published: 30 December 2024

**Citation:** Urzędowski, A.; Sachajdak, A.; Syta, A.; Zaburko, J. CFD and Statistical Analysis of the Impact of Surface Physical Parameters on the Thermal Resistance of Layered Partitions in ETICS Systems. *Energies* **2025**, *18*, 107. https://doi.org/10.3390/en18010107

## 1. Introduction

A key issue in improving the thermal insulation of buildings is the reduction of heat loss through the building envelope, which accounts for up to 25% for walls and 30% for roofs [1,2]. The mechanisms of heat transfer by conduction in single- and multi-layer walls are well-studied, investigated, and described [3,4]. However, the complex mechanism of heat transfer between rough surfaces, involving simultaneous conduction, convection, and radiation, requires further analysis [5]. Understanding heat transfer phenomena in building structures is a critical aspect from the perspective of energy efficiency and durability. Analyzing these phenomena enables the optimization of construction and insulation methods for new buildings and the improvement of retrofitting techniques for existing structures [6].

The issue of heat transfer in multilayer partitions is further complicated by their porous and heterogeneous structure. The heat transfer mechanisms in civil engineering structures described to date have not accounted for the influence of microstructure in gap regions on the contact thermal resistance of layered constructions [7–11].

This study addresses an issue not yet explored in the existing scientific literature, specifically involving the determination of the heat transfer coefficient, with a particular focus on calculating thermal contact resistance values with varying surface preparations on the side of air gaps in walls. Conducting a geometric and thermal analysis of the considered materials and their contact area provided insights into the actual thermal conditions and their impact on the insulation parameters of the building partition. In order to carry out research, authors used tools for numerical fluid mechanics, which was preceded by the construction of three-dimensional models reflecting the multi-layer building walls working conditions. Reverse engineering tools were used to reproduce the surface shape, before and after the application of reflective smoothing coating. The research focused on change in heat transport by radiation and thermal resistance in air gaps between materials and was carried out according to the chart presented in Figure 1.

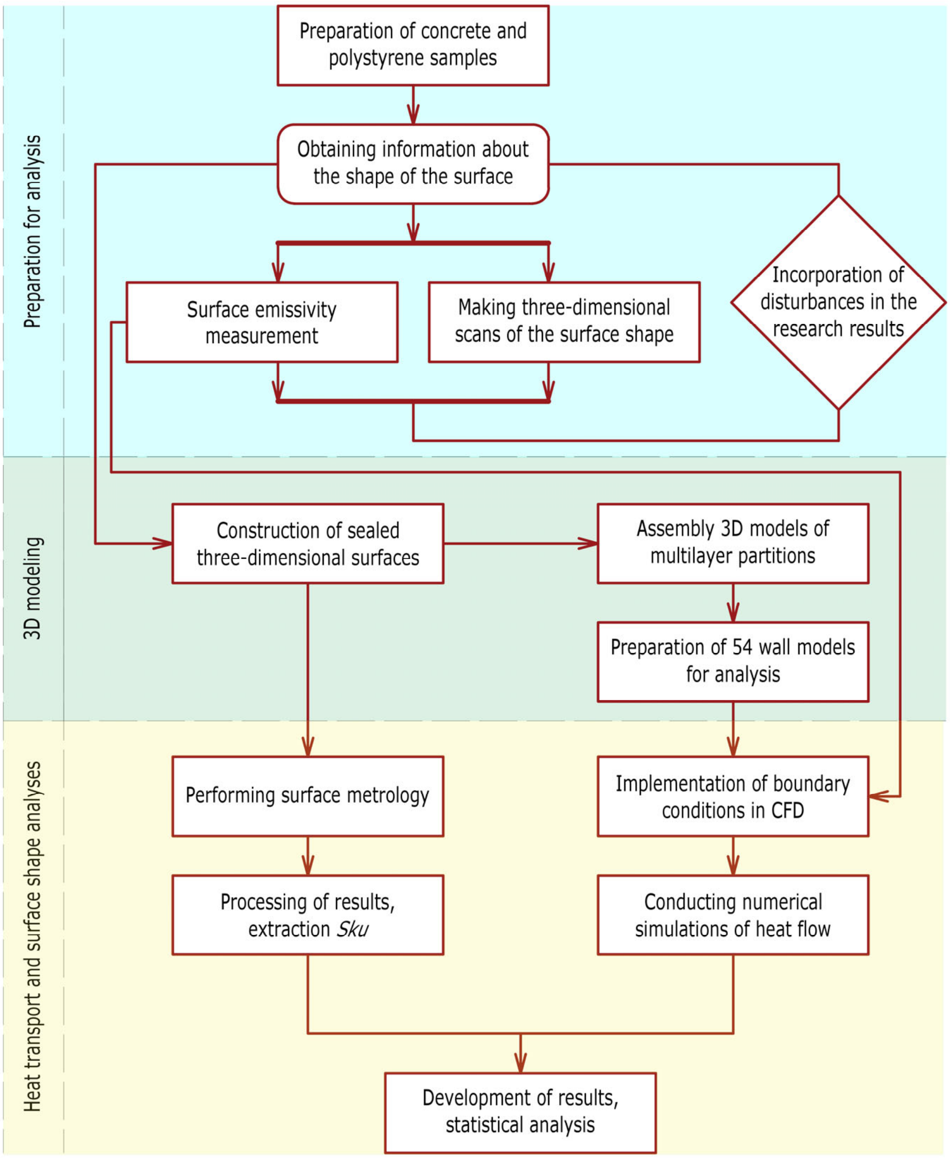

**Figure 1.** Research flow chart.

### 1.1. Thermophysical Phenomena Occurring in Multilayer Walls

In the case of the temperature distribution at specific points in a body determined solely by position T = f(x,y,z), it is referred to as steady-state heat transfer. However, if the temperature also depends on time T = f(x,y,z,τ), transient heat transfer occurs. In practice, unsteady heat transfer typically occurs in building partitions. Nevertheless, due to relatively slow in time changes of thermal and moisture conditions in typical building partitions, steady-state conduction is most often assumed. The heat flux flows exclusively in an environment with a temperature difference, from areas of higher temperature to areas of lower temperature, until equilibrium is reached [12].

Heat transfer, depending on the type of medium, can occur through [13]:

- Conduction—characteristic of solids, it is described by Fourier's law, which relates the heat flux density at a specific point in a body to the temperature gradient at that point (1):

$$q = -\lambda \nabla T \qquad \left[\mathrm{W/m^2}\right] \tag{1}$$

- Convection—characteristic of liquids and gases, the solution for fluid region bases on the continuity equation, the momentum conservation equation, and the energy equation, when heat is added to a fluid and the fluid density varies with temperature, a flow can be induced due to the force of gravity acting on the density variations. Such buoyancy-driven flows are termed natural-convection (or mixed-convection) (2)–(4) [14,15].

$$\nabla \cdot (\rho v) = 0 \tag{2}$$

$$\nabla \cdot (\rho v v) = -\nabla p + \nabla \bar{\bar{\tau}} + \rho g \tag{3}$$

$$\nabla \cdot (v \rho h) = \nabla \cdot (\lambda \nabla T + \bar{\bar{\tau}} v) \tag{4}$$

- Radiation—characteristic of solids in a gaseous medium. In this article, a two-layer vertical wall consisting of a structural layer insulated with polystyrene is analyzed, where heat transfer is realized through all three modes of exchange: conduction in the structural layer, thermal insulation and adhesive, as well as convection and radiation in the air gap [12,14], where the amount of heat exchanged by radiation from the surface to the surface (heat flux) can be described by the Formula (5):

$$Q_{1-2} = \varepsilon_{1-2} C_C \varphi_{1-2} F_1 \left[ \left( \frac{T_1}{100} \right)^4 - \left( \frac{T_2}{100} \right)^4 \right] \tag{5}$$

The thermal resistance of joints in building walls depends on several factors, including inter alia (the value of the temperature of the bodies in the contact zone, the value of the temperature of the cores of the bodies, the roughness and waviness of the surface, and the size of the joints [16–18]). In the analyzed work, the effect of changing the distance between concrete and thermal insulation was examined, which results from the technology of thermal insulation of buildings in the ETICS system [19,20]. An important role in heat transport in the air gaps is played by the emissivity of the surface, which can be modified by applying reflective and smoothing coatings used in the experiments presented in the article.

### *1.2. Problem Formulation*

The European Union committed itself to reducing the Union's economy-wide net greenhouse gas emissions by at least 55% by 2030 below 1990 levels in the updated nationally determined contribution submitted to the UNFCCC Secretariat on 17 December 2020 [21], whereas by 2050, all buildings should meet zero-energy requirements. In recent years, numerous publications have highlighted challenges related to improving the thermal performance of building envelopes to meet these requirements [22–24].

Thermal studies are being conducted on innovative materials [25], windows [26], heat transfer within multilayer walls [27] and at the joints of building envelopes [28]. Very detailed studies are conducted leading to even slight improvements, among other, research on wall corners insulated with PIR boards with aluminum facing, demonstrated that thermal coupling coefficient (L2D), with PU glue is equal to 0.2834 W/(mK), whereas without PU glue: 0.2948 W/(mK) [29]. Research on phenomena occurring in air gaps is particularly challenging due to the complexity of the processes involved, hence numerical techniques are applied to conduct analyses [30,31]. Air gap studies carried out by Saber H. H., have shown that for single and double airspaces subjected to an upward heat flow, the effective thermal resistance changed significantly with a changing $A_R$ (enclosed region aspect ratio) for the full range of effective emittance of the enclosed airspace [22]. However, previous studies on heat transfer in multilayer walls [32–34] have not accounted for thermal phenomena occurring in air gaps after modifications to the structural layer and changes in its emissivity. Authors of this article conducted research to solve and describe these issues.

To prepare the digital layered wall models, materials were collected that accurately represent the actual heat transfer phenomena occurring in vertical external building. The selected fragment represents a wall made of two layers: structural material in the form of concrete 0.24 m thick and insulating material in the form of polystyrene 0.20 m thick, which is mounted to the wall with adhesive mortar. The study did not take into account the plaster on the outside and inside of the wall, because its share is insignificant in the heat transport, it is difficult to clearly determine its thickness and it often depends on the thickness of the installations that it has to cover.

According to the ETICS (External Thermal Insulation Composite System), the thickness of the adhesive varies between 10 mm and 20 mm, and it creates an air gap in which combined heat transport is carried out by conduction, heat radiation and convection, hence, for the study, three thickness ranges have been adopted: 10, 15 and 20 mm. According to the guidelines [20,35], the adhesive mortar is applied to polystyrene boards using the circumferential point method, as a result of which it fills approx. 35% of the board surface, while the rest is filled with air. For better illustration of the phenomena occurring in the air gaps, a fragment of thickness between 70 and 80 mm (depending on the width of the gap) and an area of 0.1 $m^2$ was distinguished for further analysis (Figure 2).

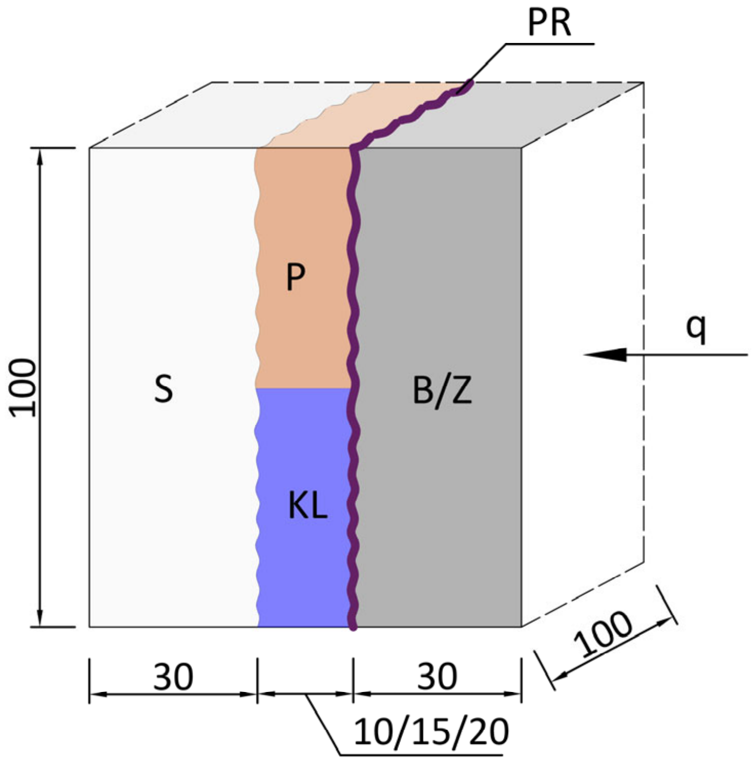

**Figure 2.** Model of a section of the layered wall subjected to testing.

The following material designations were adopted:

| | |
|---|---|
| B | concrete R.23; |
| Z | concrete R.23.1; |
| S | polystyrene; |
| KL | adhesive mortar for polystyrene; |
| P | air; |
| PR | reflective smoothing coating, acrylic enamel spray. |

Samples, as well as the components of the R.23 and R23.1 concrete mixtures, were obtained from the company, which specializes in the production of pre-casting elements for residential, industrial and road construction. The formulation of the analyzed R23 and R23.1 concretes was developed as part of research and development activities within the company, focusing on the production of innovative, architectural self-compacting concrete mixtures. The difference in the composition of the concrete mix R23 and R23.1 consisted of reducing the superplasticizer from 3.1 to 2.9 kg/m$^3$ and adding the ingredient bonding accelerator in the amount of 2.3 kg/m$^3$, which resulted in increased workability of the mix.

Thermal analyses were conducted on 54 samples in the simulation studies which preceded categorized by concrete, gap thickness, and filling of the gap between the layers, and were summarized in Table 1. Wall layer systems were divided into three groups, assigned a code to facilitate statistical analyses. Each code included three samples with structural layers made from Z-type concrete and three with B-type concrete. The differences between them resulted from the filling of the space between the thermal insulation and the structural layer, which was denoted by the symbol *d*, with an adopted value of 10, 15 or 20 mm. In the system described by code 0, the closed gap is filled with air where no turbulent fluid motion occurs. In the Code 1 model, the space is filled with adhesive, and heat transfer occurs exclusively through conduction. In contrast, the Code 2 model replicates a configuration with an air-filled gap, where the structural layer is additionally coated with a reflective-smoothing layer. Prior to computer simulations, the CFD environment was configured to incorporate the physical properties of the samples, environmental conditions, and thermal resistances, following thermophysical algorithms derived from laboratory research. Both systems accounted for variations in the gap thickness between the thermal insulation layer and the structural layer within the specified ranges analyzed in this study.

**Table 1.** Analyzed layered wall systems, classified by code, type of concrete and air gap thickness.

| **Code** | **0** | | **1** | | **2** | |
|---|---|---|---|---|---|---|
| **Concrete Type** | **Z1** | **B1** | **Z1** | **B1** | **Z1** | **B1** |
| d = 0.01 m | Z1+P10+S | B1+P10+S | Z1+KL10+S | B1+KL10+S | Z1+PR+P10+S | B1+PR+P10+S |
| | Z1+P10+S | B2+P10+S | Z2+KL10+S | B2+KL10+S | Z2+PR+P10+S | B2+PR+P10+S |
| | Z1+P10+S | B3+P10+S | Z3+KL10+S | B3+KL10+S | Z3+PR+P10+S | B3+PR+P10+S |
| d = 0.015 m | Z1+P15+S | B1+P15+S | Z1+KL15+S | B1+KL15+S | Z1+PR+P15+S | B1+PR+P15+S |
| | Z2+P15+S | B2+P15+S | Z2+KL15+S | B2+KL15+S | Z2+PR+P15+S | B2+PR+P15+S |
| | Z3+P15+S | B3+P15+S | Z3+KL15+S | B3+KL15+S | Z3+PR+P15+S | B3+PR+P15+S |
| d = 0.02 m | Z1+P20+S | B1+P20+S | Z1+KL20+S | B1+KL20+S | Z1+PR+P20+S | B1+PR+P20+S |
| | Z2+P20+S | B2+P20+S | Z2+KL20+S | B2+KL20+S | Z2+PR+P20+S | B2+PR+P20+S |
| | Z3+P20+S | B3+P20+S | Z3+KL20+S | B3+KL20+S | Z3+PR+P20+S | B3+PR+P20+S |

### *1.3. Modification of Heat Transfer by Radiation Through the Reduction of Surface Irregularities*

It is a well-known phenomenon that the emissivity of a surface depends strongly on its roughness. Agabov [36,37] developed a simple yet effective method for determining the emissivity of rough surfaces with uniform thermal and reflective properties. As shown in Figure 3, he modeled local surface roughness as a depression in area $A_r$ and examined the total radiation leaving the ideally smooth reference surface $A_s$, taking into account the effects of reflections from the actual surface $A_r$ [36].

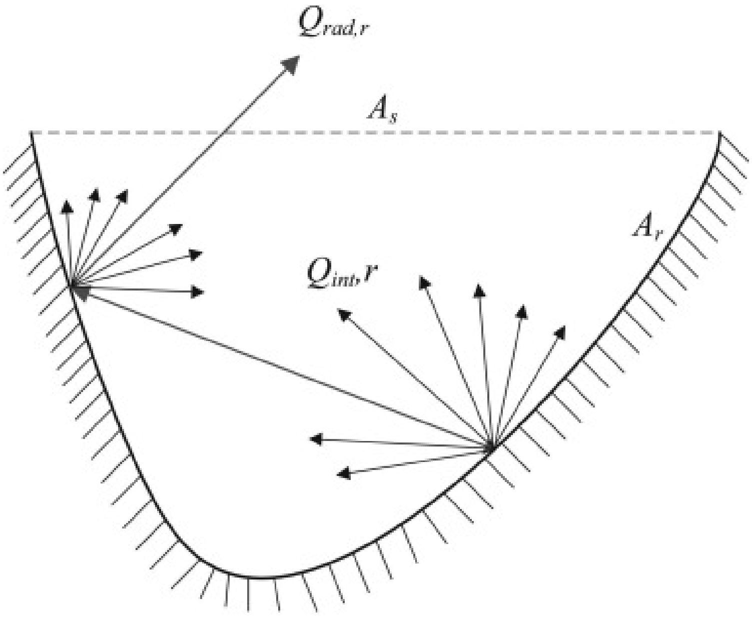

**Figure 3.** Modeling the behavior of incident flux on surface irregularities [36].

Agababov described the relationship between the emissivity of a gray body's surface and its geometry using the Formula (6):

$$\varepsilon_r = \left[1 + \left(\frac{1}{\varepsilon_s} - 1\right) R_{rs}\right]^{-1} \tag{6}$$

where the roughness coefficient of the gray body $R_{rs}$ is (7):

$$R_{rs} = \frac{A_s}{A_r} \tag{7}$$

For a rectangular cavity with side length $l$, where the surface area $A_s$ is $l^2$, and the surface $A_r$ is discretized into $M$-micro-surfaces, the roughness of the body is expressed by the Formula (8):

$$R_{rs} = \frac{l^2}{\sum_{i=1}^{M} A_{ri}} \tag{8}$$

Based on these relationships and working with three-dimensional models, Zezhan [37] proposed a method for determining surface emissivity that accounts for its roughness in three steps:

1. measuring the root mean square roughness $S_q$,
2. determining $A_r$ and calculating the coefficient $R_{rs}$ from Formula (8),
3. calculating $\varepsilon_s$ of the reference surface.

### 1.4. Solving Thermal Problems of Heat Transfer in CFD

Numerical fluid mechanics, or computational fluid dynamics (CFD), is a method used to solve equations describing fluid flow, system behaviors, heat transfer, mass transfer, and other similar physical phenomena [38–40]. Its application provides essential information on the distribution of velocity fields, pressure fields, heat movement, temperature fields, and other associated phenomena [28,41–43]. CFD enables the analysis of issues without the need for time-consuming and costly experimental studies [44–46]. However, simulation studies should be preceded by verification and validation of the model under real or laboratory conditions. CFD methods are applied in simulations of pressure drops during fluid flow, lift forces on aircraft wings, rotor thrust, airflow in air conditioning systems, temperature distribution in rooms, mixing processes, and more [28,47–49].

The Ansys Fluent program was chosen for thermal calculations due to its advanced calculation engine, module that allows it to import 3D geometry from reverse engineering programs and module for determining the results of calculations taking into account heat transfer paths. The phenomena occurring in the partition were calculated using the finite volume method (FVM), which is a numerical technique that converts volume integrals with divergence terms into surface integrals using the divergence theorem [25,50]. This allows for partial differential equations to be expressed and solved as algebraic equations within the FVM framework.

## 2. Materials and Methods

### 2.1. Collection of Geometric Data on the Concrete Surface Before and After the Application of the Reflective Smoothing Coating

Three-dimensional surface measurements of the samples (Figure 4a) were performed using the ATOS Core 3D optical scanner, (LENSO SP. Z O.O., Poznań, Poland) with a single scan field of 0.2 × 0.15 m, camera resolution of 5 MP, and sensor dimensions of 0.21 × 0.21 × 0.06 m. Data collection (points in space) was carried out using triangulation and recorded in GOM Scan software (2019, GOM GmbHa ZEISS, Braunschweig, Germany), where the point cloud was processed into a triangular mesh (polygonization).

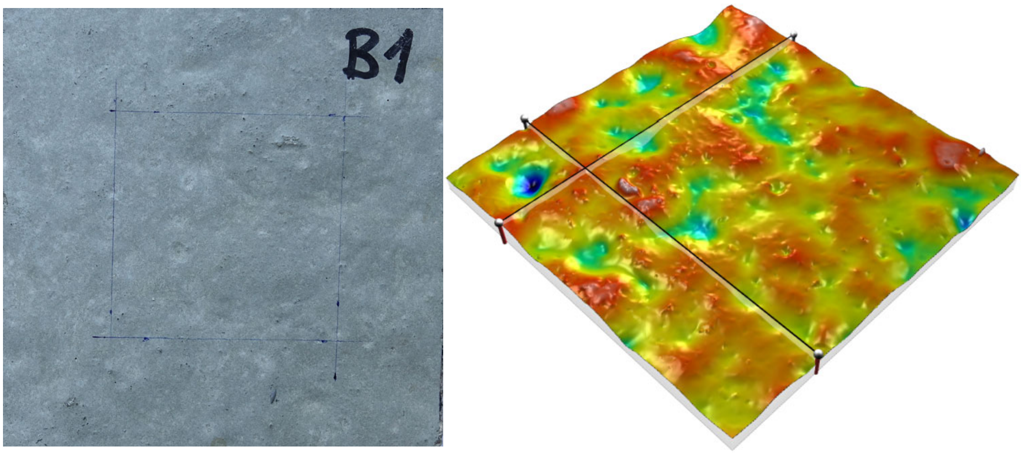

(**a**) (**b**)

**Figure 4.** Sample B1: (**a**) view of B1 sample surface, (**b**) an isometric view of the 3D scanned model of B1 sample surface with a color-coded interpretation of depressions and peaks.

Surface metrology of the scanned samples was conducted based on representative point clouds using MountainsLab Premium software by Digital Surf, version 8.1. Detailed morphometric measurements, geometric profiles, roughness analysis, assessments of surface waviness and spatial locations of these phenomena were performed [51]. Parameters defining surface topography, including height, frequency, hybrid, and functional characteristics were also determined [51–53]. Advanced software options allowed for the visualization of 3D surfaces in 24-bit resolution with real-time manipulation. Rendering with color palettes was applied (Figure 4b) and measurement data were cleaned using an advanced filter to remove anomalies, which facilitated the detection of surface features and potential irregularities.

After scanning and conducting surface structure analysis, sheet piling meshes have been converted into solids from which the models of multilayer walls were assembled in 3D computer-aided design software. Models consisting of three solids representing: concrete, polystyrene and air have been converted to .sat format and implemented to the environment of computational fluid mechanics in order to conduct heat transfer simulations.

The emissivity of the surface was examined using a custom-designed and constructed setup, which consisted of a measurement system: Flir T440bx thermal imaging camera (Teledyne FLIR LLC., Wilsonville, OR, USA) mounted on a tripod, an enclosure to limit ambient emissions and point reflections, a heating system with a thermostat to raise the sample surface temperature by 20 °C, and a multi-channel temperature recorder with probes [53]. Research methodology was based on guidelines provided in the literature, the FLIR device manual, and the instructions from the FLIR Tools/Tools+ software manual [54,55].

### *2.2. Boundary Conditions Implemented into the Model in the Computer Fluid Dynamics Program*

For heat transport calculations using numerical fluid dynamics, the Ansys Fluent program (2020 R1) was used, which conducted the thermal issues considered in the article using the finite volume method. The simulation was preceded by importing the wall model, describing the model, assigning physical properties of materials and describing the model into finite volumes (Figure 5a). The volume of geometrical model is divided into 33 million cells using periodic system at the side surfaces for reducing size of the model but with regards to wider area of real multilayer wall at the buildings. A stationary tetrahedral non-structural mesh is used for calculations, as shown in the Figure 5a. That type of mesh allows for a simplified process of mesh creation compared to structural mesh which can be difficult to process at unregular scanned surfaces. The mesh density is mainly due to the irregularity of the scanned surfaces. Because the important role of natural convection is expected inside the air gap, the proper wall layer was created with five layers with the inflation coefficient set to 1.1. Y+ boundary layer thickness takes values below 20. Default parameters of k-w were assumed.

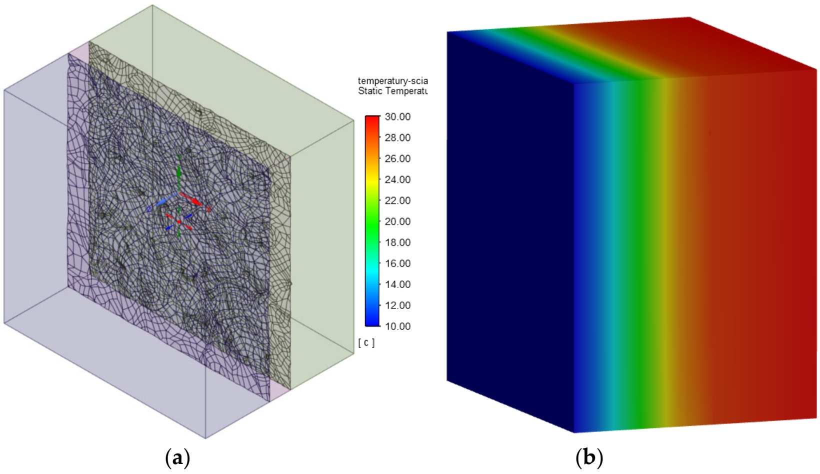

(**a**) (**b**)

**Figure 5.** Model of multilayer partition with representation of the surface shape in the CFD program window: (**a**) during mesh discretization, (**b**) visualization of temperature distribution after performing heat transport simulations.

Boundary conditions are assumed as follows:

- wall temperature at the warm side of the wall t = 30 °C,
- wall temperature at the cold side of the wall t = 10 °C,
- periodic boundary condition at the side surfaces of the air gap,
- heat flux equal to 0 at the side surfaces of the solid regions (pseudo one-dimensional heat transfer in solid regions),
- coupled heat transfer at the inner surfaces of the air gap with the emissivity assumed, respectively.

Results of the simulation were converted into the values of the heat transfer coefficient and thermal resistance of each layer, and after post-processing, they were presented in a graphic form with visualization of temperature distribution (Figure 5b).

For a diffuse surface, the reflectivity is independent of the incidence and reflection directions. In models analyzed in the paper, in which the space between the layers is filled with air, the equation transport (5) for flux leaving the surface $k$ is determined in the Ansys [56–58] from (9):

$$q_{out,s} = \varepsilon_s \sigma T_k^4 + \rho_k + q_{in,k} \tag{9}$$

The turbulent flow model has been adopted with a model $k - \omega$ SST, which combines the advantages of the model $k - \varepsilon$ and model $k - \omega$, and introduces an additional component limiting the overproduction of kinetic energy of turbulence in areas of strong positive pressure gradients (dam points, areas of detachment of the boundary layer) [59,60]. The assumed model of the real gas-air is an incompressible ideal gas, in which the density is determined from the Clapeyron ideal gas equation [61,62]. The radiative heat flow for the air void was determined using the S2S (surface-to-surface) model [63]. The S2S radiation model in Ansys assumes that surfaces are diffusible. The emissivity and absorption of the grey surface is independent of the wavelength, and according to Kirchoff's law, they are equal ($\varepsilon = \alpha$) [10,64,65].

### 2.3. Collection and Processing of Results from the CFD Analyses

For the purpose of determining the heat transfer coefficient of the analyzed wall models, formulas for $U$ (10) were derived taking into account the total heat flux $\dot{Q}$, which is obtained from the numerical analyses conducted.

$$U = \frac{\dot{Q}}{A} / (T_1 - T_2) \tag{10}$$

To determine the U-value, it was also necessary to obtain information on the interior and exterior surface temperatures of the component and implement the physical properties of the models, which values for B1+P20+S model was recorded and presented in Table 2. Using computational fluid dynamics (CFD) tools, it was also possible to identify the heat transport paths and determine the value of the heat flux transferred through radiation $\dot{Q}_{RAD}$.

For the accurate interpretation of the impact of changes in the emissivity of the construction layer's surface on thermal phenomena occurring in the analyzed walls, it was necessary to determine the thermal resistances in the air gaps between the concrete and the thermal insulation using Equation (11):

$$R_S = \frac{(A \cdot \Delta T)}{\dot{Q}} \tag{11}$$

where

$$\Delta T = T_{B\_SRC} - T_{S\_TRG}$$

**Table 2.** Summary of results and parameters implemented into the algorithms in order to determine and compare the U of partitions, for the model in the B1+P20+S configuration.

| | | |
|---|---|---|
| $\dot{Q}$ | W | 0.1778 |
| $\dot{Q}_{RAD}$ | W | 0.1221 |
| $A$ | m2 | 0.009 |
| $d$ | m | 0.08 |
| $T_1$ | °C | 30 |
| $T_2$ | °C | 10 |
| $U$ | W/m$^2$K | 0.9852 |
| $\lambda_z$ | W/mK | 0.079 |

For each of the 54 analyzed cases, calculations were performed according to Formulas (6) and (7), which were compiled in spreadsheets presented for a selected model constructed of B1 concrete without a coating and with a 20 mm air gap between the structural layer and the polystyrene (Table 3).

**Table 3.** Summary of the results and parameters implemented in the algorithms to determine the thermal resistances of gaps, for model in the B+P20+S configuration.

| | | |
|---|---|---|
| $\dot{Q}$ | W | 0.1778 |
| $T_{B\_SRC}$ | °C | 29.3 |
| $T_{S\_TRG}$ | °C | 26.3 |
| $\Delta T$ | °C | 3.0 |
| $A$ | m$^2$ | 0.009 |
| $R_S$ | (m$^2$K)/W | 0.1513 |

### 2.4. Determination of Samples Roughness Parameters

Among parameters describing surface roughness, four groups can be distinguished: hybrids, volumes, functional and heights in which the most important for the course of thermal phenomena considered in the work in terms of emissions are: *Sq* and *Sku*. *Sku* is the kurtosis of the 3D surface texture, respectively [3,66]. Figuratively, a histogram of the heights of all measured points is established and the symmetry and deviation form an ideal normal (i.e., bell curve) distribution, while mathematically, it is evaluated as follows (12) and (13):

$$S_{ku} = \frac{1}{S_q^4}\sqrt{\iint_a \left(Z(x,y)^4\right)dxdy} \tag{12}$$

where:

$$S_q = \sqrt{\iint_a \left(Z(x,y)^2\right)dxdy} \tag{13}$$

*Sku* indicates the presence of inordinately high peaks/deep valleys (*Sku* > 3.00) or lack thereof (*Sku* < 3.00) making up the texture. If the surface heights are normally distributed (i.e., bell curve), then *Ssk* is 0.00 and *Sku* is 3.00. Surfaces described as gradually varying, free of extreme peaks or valley features, will tend to have *Sku* < 3.00.

*Sq*, root mean square roughness, is evaluated over the complete 3D surface, respectively. It represent an overall measure of the texture comprising the surface and is insensitive in differentiating peaks, valleys and the spacing of the various texture features [67].

Thus, *Sq* may be misleading in that many surfaces with grossly different spatial and height symmetry features (e.g., milled vs. honed) may have the same *Sq*, but function quite differently [68].

The results of the analysis of surface roughness before and after applying the reflective coating indicate a significant, nearly tenfold, reduction in the depressions and peaks on the concrete surface after the application of the coating (Table 4). These results may have a significant impact on heat transfer because the reflection of radiation on smooth surfaces is specular, whereas on matte surfaces it is diffuse and more readily absorbed.

**Table 4.** Change in the height parameters of the B1 sample surface before and after applying a reflective and smoothing coating.

| **Parameter** | | | **B1** | | **Z1** | |
|---|---|---|---|---|---|---|
| | | | | **+PR** | | **+PR** |
| Root Mean Square Roughness | $S_q$ | µm | 1.88 | 4.20 | 2.47 | 5.52 |
| Kurtosis of the 3D surface texture | $S_{ku}$ | | 4.47 | 0.55 | 5.62 | 0.69 |

# 3. Results

## 3.1. Development and Presentation of the Overall Research Results

The application of a low-emissivity coating on the concrete surface adjacent to the polystyrene layer significantly improves the thermal insulation properties of the entire partition and reduces the wall's thermal transmittance coefficient.

After applying the reflective and smoothing coating, the U-value of thermal transmittance for models constructed with B-type concrete was reduced by 27.8% for a 10 mm air gap, 38.1% for a 15 mm gap, and 42.1% for a 20 mm gap (Figure 6a). Thus, the average reduction in the U-value of thermal transmittance achieved for the analyzed layered partition models was 36.0%. Similarly, after applying the reflective and smoothing coating, the U-value of thermal transmittance for models constructed with Z-type concrete was reduced by 28.2% for a 10 mm air gap, 38.7% for a 15 mm gap, and 43.0% for a 20 mm gap (Figure 6b). Consequently, the average reduction in the U-value of thermal transmittance achieved for the analyzed layered partition models was 36.6%.

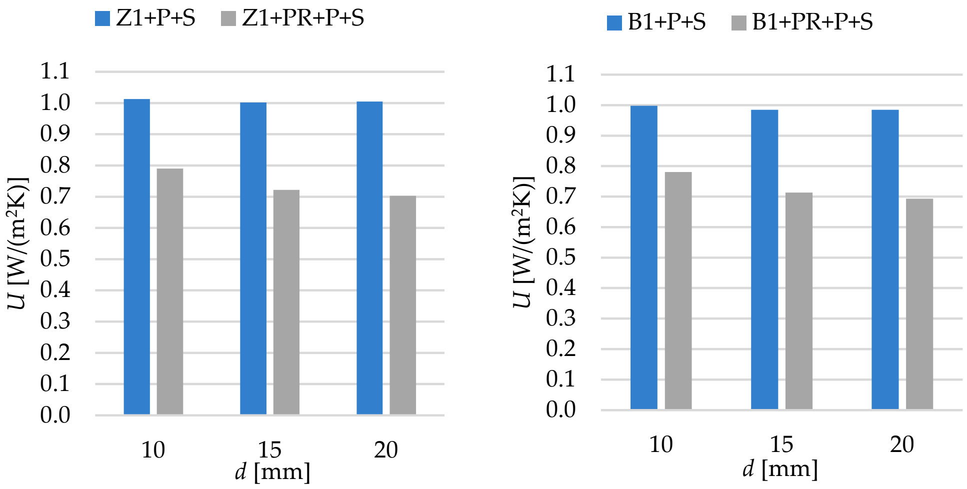

(**a**) (**b**)

**Figure 6.** Change in heat transfer coefficient *U* of multilayered wall models after applying a reflective coating: (**a**) to the concrete surface B1, (**b**) to the concrete surface Z1.

For both layered models with B-type and Z-type concrete, the U-value is lowest when the distance between the structural layer and the thermal insulation is 15 mm (Figure 7). A slight correlation was observed between changes in the thickness of the air-filled gap and the U-value. In the B+P+S models, reducing the gap thickness to 10 mm resulted in an increase in the thermal transmittance coefficient by 1.3%, while increasing the gap thickness to 20 mm caused a 1.3% increase compared to models with a 15 mm gap. Similarly, for the Z+P+S models, reducing the gap from 15 mm to 10 mm led to a 1.1% increase in the thermal transmittance coefficient, whereas a gap thickness of 20 mm resulted in a 0.9% increase compared to models with a 15 mm gap.

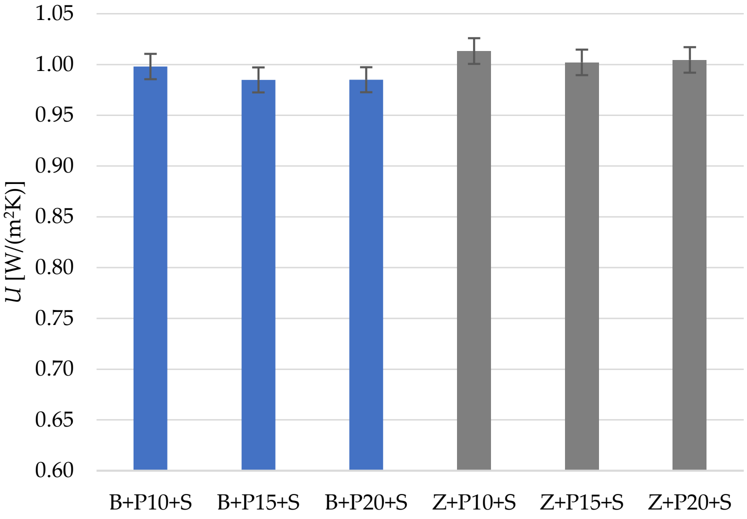

**Figure 7.** Change in heat transfer coefficient of multilayered wall models depending on the air gap thickness.

To investigate the statistically significant differences in heat transfer across various constructions, the following parameters were used: thermal resistance of the wall, thermal resistance of the air gap, categorize the models based on the gap-filling material, air gap thickness, emissivity of the concrete surface involved in radiative heat exchange, kurtosis of the 3D surface texture (Table 5). For each studied characteristic, a representative number of eighteen samples was used. Identical measurement conditions were ensured for all samples. The analyses considered simulation results conducted in a computational fluid dynamics environment on layered component models in the baseline configuration (Table 1) and the results of the heat transport studies are presented in Table 5. The measurements exhibit a certain degree of variability.

**Table 5.** Comparison of parameters of surface type B1 before and after applying a reflective and smoothing coating.

| No. | Type | Class | *d* [m] | *Rs* [(m$^2$K)/W] | *Rp* [(m$^2$K)/W] | *ε* | *Sku* |
|---|---|---|---|---|---|---|---|
| 1 | Z1+P10+S | 0 | 10 | 0.1311 | 0.9872 | 0.93 | 5.616 |
| 2 | Z2+P10+S | 0 | 10 | 0.1295 | 0.9867 | 0.93 | 14.079 |
| 3 | Z3+P10+S | 0 | 10 | 0.1296 | 0.9870 | 0.93 | 9.802 |
| 4 | Z1+P15+S | 0 | 15 | 0.1474 | 0.9982 | 0.93 | 5.616 |
| 5 | Z2+P15+S | 0 | 15 | 0.1474 | 0.9978 | 0.93 | 14.079 |
| 6 | Z3+P15+S | 0 | 15 | 0.1472 | 0.9979 | 0.93 | 9.802 |
| 7 | Z1+P20+S | 0 | 20 | 0.1504 | 0.9956 | 0.93 | 5.616 |
| 8 | Z2+P20+S | 0 | 20 | 0.1505 | 0.9956 | 0.93 | 14.079 |
| 9 | Z3+P20+S | 0 | 20 | 0.1503 | 0.9954 | 0.93 | 9.802 |

**Table 5.** *Cont.*

| No. | Type | Class | *d* [m] | *Rs* [(m$^2$K)/W] | *Rp* [(m$^2$K)/W] | *ε* | *Sku* |
|---|---|---|---|---|---|---|---|
| 10 | Z1+KL10+S | 1 | 10 | 0.0228 | 0.9921 | 0.93 | 5.616 |
| 11 | Z2+KL10+S | 1 | 10 | 0.0227 | 0.9921 | 0.93 | 14.079 |
| 12 | Z3+KL10+S | 1 | 10 | 0.0228 | 0.9921 | 0.93 | 9.802 |
| 13 | Z1+KL15+S | 1 | 15 | 0.0343 | 1.0063 | 0.93 | 5.616 |
| 14 | Z2+KL15+S | 1 | 15 | 0.0342 | 1.0062 | 0.93 | 14.079 |
| 15 | Z3+KL15+S | 1 | 15 | 0.0342 | 1.0063 | 0.93 | 9.802 |
| 16 | Z1+KL20+S | 1 | 20 | 0.0457 | 1.0204 | 0.93 | 5.616 |
| 17 | Z2+KL20+S | 1 | 20 | 0.0456 | 1.0204 | 0.93 | 14.079 |
| 18 | Z3+KL20+S | 1 | 20 | 0.0457 | 1.0204 | 0.93 | 9.802 |
| 19 | Z1+PR+P10+S | 2 | 10 | 0.2440 | 1.2663 | 0.29 | 0.691 |
| 20 | Z2+PR+P10+S | 2 | 10 | 0.2425 | 1.2623 | 0.29 | 1.732 |
| 21 | Z3+PR+P10+S | 2 | 10 | 0.2445 | 1.2670 | 0.29 | 1.206 |
| 22 | Z1+PR+P15+S | 2 | 15 | 0.2900 | 1.3851 | 0.29 | 0.691 |
| 23 | Z2+PR+P15+S | 2 | 15 | 0.2889 | 1.3814 | 0.29 | 1.732 |
| 24 | Z3+PR+P15+S | 2 | 15 | 0.2904 | 1.3856 | 0.29 | 1.206 |
| 25 | Z1+PR+P20+S | 2 | 20 | 0.2940 | 1.4236 | 0.29 | 0.691 |
| 26 | Z2+PR+P20+S | 2 | 20 | 0.2933 | 1.4214 | 0.29 | 1.732 |
| 27 | Z3+PR+P20+S | 2 | 20 | 0.2942 | 1.4246 | 0.29 | 1.206 |
| 28 | B1+P10+S | 0 | 10 | 0.1319 | 1.0017 | 0.93 | 4.470 |
| 29 | B2+P10+S | 0 | 10 | 0.1316 | 1.0018 | 0.93 | 9.283 |
| 30 | B3+P10+S | 0 | 10 | 0.1322 | 1.0024 | 0.93 | 7.213 |
| 31 | B1+P15+S | 0 | 15 | 0.1474 | 1.0154 | 0.93 | 4.470 |
| 32 | B2+P15+S | 0 | 15 | 0.1474 | 1.0155 | 0.93 | 9.283 |
| 33 | B3+P15+S | 0 | 15 | 0.1475 | 1.0156 | 0.93 | 7.213 |
| 34 | B1+P20+S | 0 | 20 | 0.1513 | 1.0150 | 0.93 | 4.470 |
| 35 | B2+P20+S | 0 | 20 | 0.1513 | 1.0154 | 0.93 | 9.283 |
| 36 | B3+P20+S | 0 | 20 | 0.1514 | 1.0153 | 0.93 | 7.213 |
| 37 | B1+KL10+S | 1 | 10 | 0.0229 | 0.9985 | 0.93 | 4.470 |
| 38 | B2+KL10+S | 1 | 10 | 0.0228 | 0.9984 | 0.93 | 9.283 |
| 39 | B3+KL10+S | 1 | 10 | 0.0228 | 0.9984 | 0.93 | 7.213 |
| 40 | B1+KL15+S | 1 | 15 | 0.0343 | 1.0126 | 0.93 | 4.470 |
| 41 | B2+KL15+S | 1 | 15 | 0.0342 | 1.0126 | 0.93 | 9.283 |
| 42 | B3+KL15+S | 1 | 15 | 0.0343 | 1.0126 | 0.93 | 7.213 |
| 43 | B1+KL20+S | 1 | 20 | 0.0457 | 1.0268 | 0.93 | 4.470 |
| 44 | B2+KL20+S | 1 | 20 | 0.0457 | 1.0268 | 0.93 | 9.283 |
| 45 | B3+KL20+S | 1 | 20 | 0.0457 | 1.0268 | 0.93 | 7.213 |
| 46 | B1+PR+P10+S | 2 | 10 | 0.2454 | 1.2812 | 0.29 | 0.551 |
| 47 | B2+PR+P10+S | 2 | 10 | 0.2444 | 1.2790 | 0.29 | 1.142 |
| 48 | B3+PR+P10+S | 2 | 10 | 0.2453 | 1.2812 | 0.29 | 0.887 |
| 49 | B1+PR+P15+S | 2 | 15 | 0.2908 | 1.4024 | 0.29 | 0.551 |
| 50 | B2+PR+P15+S | 2 | 15 | 0.2901 | 1.4008 | 0.29 | 1.142 |
| 51 | B3+PR+P15+S | 2 | 15 | 0.2908 | 1.4026 | 0.29 | 0.887 |
| 52 | B1+PR+P20+S | 2 | 20 | 0.2950 | 1.4432 | 0.29 | 0.551 |
| 53 | B2+PR+P20+S | 2 | 20 | 0.2946 | 1.4422 | 0.29 | 1.142 |
| 54 | B3+PR+P20+S | 2 | 20 | 0.2951 | 1.4434 | 0.29 | 0.887 |

CFD analysis, by its nature, is time-intensive and demands significant computational resources. Direct application of CFD tools to building thermal design or control poses numerous challenges. A potential solution lies in translating CFD results into efficient statistical models. Differentiation between various material configurations (Classes 0, 1, 2) can be achieved using statistical methods and artificial intelligence. In this context, group statistical tests for data distribution and machine learning classification models prove to be particularly valuable.

### 3.2. Statistical Analysis

Preliminary comparison of variable distributions across individual groups can be conducted using box plots. These plots graphically present central tendencies, variability, and skewness of the data. A box plot illustrates the median (line inside the box), skewness as the position of the median, dispersion as the interquartile range (IQR, length of the boxes), and outliers (points outside the whiskers). The box plots of the *Rs*, *Rp* and *Sku* values summarized in Table 5 are presented in Figure 8.

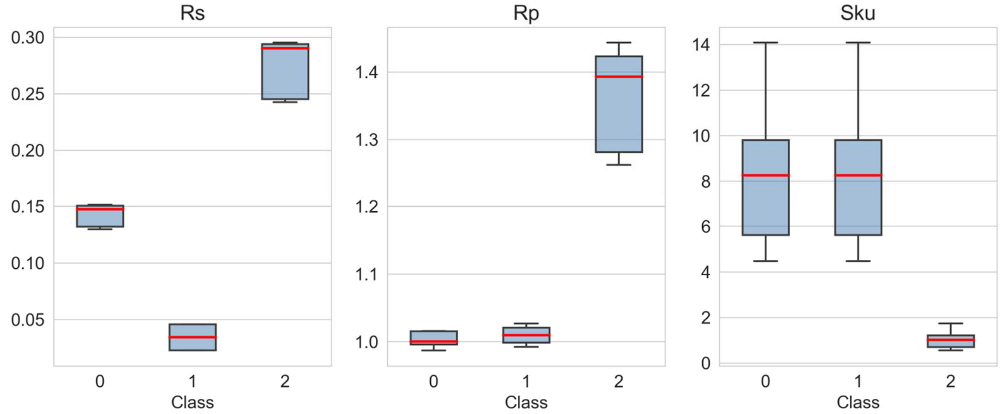

**Figure 8.** The box plots of the input data set.

The tabular summary of independent variables (Table 5) shows a finite set of values taken by the variables d (three values) and eps (two values) for all values of the dependent variable (Class). This means that they do not introduce additional information to the analysis and can be excluded from it. For the remaining independent variables (Figure 6), the largest statistical differences occur for the *Rs* values, clearly distinguishing all three classes (0, 1, and 2). The *Rp* values also allow for distinguishing the individual classes, but the differences between class 0 and 1 are less noticeable. Meanwhile, the *Sku* values show differences only for two groups (0–1 and 2). Nevertheless, it is worth emphasizing that even simple descriptive statistics, presented graphically in the form of box plots, show significant differences in the case of material configuration with an air gap and an additional reflective-smoothing coating (class 2).

More information regarding the statistical differences between observations can be provided by statistical tests. Here, the non-parametric Kruskal–Wallis test was chosen, which is used to compare at least two independent groups. This test is an alternative to one-way ANOVA but does not assume normality of the data distribution. Using the implementation of the Kruskal–Wallis test from the scipy package (Scipy v1.14.1), we compared the groups of features *Rs, Rp*, and *Sku*. At a significance level of $\alpha = 0.01$, the null hypothesis (H0) was formulated as follows: the medians of all groups are equal, indicating no significant differences between the groups in terms of the median. Conversely, the alternative hypothesis (H1) posits that at least one of the groups differs in median from the others, suggesting significant differences between the groups in terms of the median. Given the *p*-value of ($8.96 \times 10^{-27}$) at a significance level of $\alpha = 0.01$, we can reject the null hypothesis (H0). This extremely low p-value indicates that there are significant differences between the groups in terms of their medians.

## 4. Conclusions

Surface metrology has shown that the application of a reflective-smoothing coating significantly affects the configuration of the surface microstructure, particularly the kurtosis of the 3D surface texture, resulting in an almost tenfold reduction in irregularities on average, which have a direct impact on the emissivity of the surface, which was reduced from 0.93 to 0.29. Thermal analyses conducted have shown that, in accordance with transport phenomena theory, there is a significant reduction in the density of heat flux exchanged through radiation in air gaps, by approximately 86%, which resulted in a 28% improvement of the evaluated walls samples. This approach enables the enhancement of wall thermal insulation while simultaneously reducing their thickness, making it particularly applicable in the construction industry, especially for prefabricated sandwich panels.

Heat transfer in the analyzed, closed air gaps between concrete and thermal insulation occurs primarily through radiation. The thickness of the gap affects the heat exchange phenomena. The studies have shown that for the Z+P+S models, increasing the gap thickness from 10 mm to 15 mm results in a thermal resistance increase average of 13%, and from 15 mm to 20 mm of 2%. After applying the reflective and smoothing coating, these values were 18% and 1%, respectively. For models constructed from Z concrete, the proportions were very similar. This leads to the conclusion that increasing the air gap thickness from 10 mm to 15 mm is more advantageous, as it is associated with the occurrence of convective movements in larger gaps, and the coating enhances thermal insulation of walls.

A further research direction is to conduct CFD simulations and explore statistical correlations between changes in the surface emissivity of polystyrene through the application of a reflective coating and variations in thermal resistance within the air gaps of multilayer walls. This approach could be implemented in practice at the stage of production of ETICS system components, increasing the availability of the solution.

**Author Contributions:** Conceptualization, A.S. (Andrzej Sachajdak); Methodology, A.U. and A.S. (Andrzej Sachajdak); Software, A.U., A.S. (Andrzej Sachajdak) and J.Z.; Validation, A.U.; Formal analysis, A.U., A.S. (Andrzej Sachajdak) and A.S. (Arkadiusz Syta); Investigation, A.U.; Resources, A.U.; Data curation, A.S. (Arkadiusz Syta); Writing—original draft, A.U.; Writing—review & editing, A.S. (Andrzej Sachajdak), A.S. (Arkadiusz Syta) and J.Z.; Visualization, J.Z.; Supervision, A.S. (Andrzej Sachajdak). All authors have read and agreed to the published version of the manuscript.

**Funding:** The study was funded by research grants from the Polish Ministry of Education and Science in Warsaw, Poland: FD-20/IS-6/050; The study was funded by research grants from the Polish Ministry of Education and Science in Warsaw, Poland: FN-52.

**Data Availability Statement:** The original contributions presented in the study are included in the article, further inquiries can be directed to the corresponding author.

**Conflicts of Interest:** The authors declare no conflict of interest.

## Nomenclature

| | |
|---|---|
| $A_s$ | surface area [m$^2$], |
| $C_C$ | blackbody radiation coefficient equal to 5.77 [W/(m$^2$K)], |
| $d$ | air gap thickness [m], |
| $g$ | gravitational vector, |
| $h$ | enthalpy [J/kg], |
| $l$ | length, |
| $p$ | static pressure [Pa], |
| $q$ | heat flux density [W/m$^2$], |
| $q_{in,k}$ | flux of energy incident on the surface from the environment [W/m$^2$], |
| $q_{out,k}$ | flux of energy leaving the surface [W/m$^2$], |
| $R_p$ | thermal resistance of the wall [(m$^2$K)/W], |
| $R_s$ | thermal resistance of the air gap [(m$^2$K)/W], |
| $R_{rs}$ | roughness coefficient of the gray body, |

| | |
|---|---|
| $S_{ku}$ | kurtosis of the 3D surface texture, |
| $S_q$ | root mean square roughness [mm], |
| $T$ | temperature [K], |
| $T_1$ | interior surface temperature [K], |
| $T_2$ | exterior surface temperature [K], |
| $T_{B\_SRC}$ | surface temperature of the concrete on the air gap side [K], |
| $T_{S\_TRG}$ | surface temperature of the polystyrene on the air gap side [K]. |
| *Greek symbols* | |
| $\varepsilon_s$ | surface emissivity, |
| $\varepsilon_{1-2}$ | equivalent emissivity, |
| $\lambda$ | thermal conductivity [W/(mK)], |
| $\rho$ | density [kg/m$^3$], |
| $\overline{\overline{\tau}}$ | stress tensor, |
| $v$ | velocity vector, |
| $\varphi_{1-2}$ | configuration ratio. |
| *Acronyms* | |
| CAD | Computer Aided Design, |
| CFD | Computational Fluid Dynamics, |
| EPS | Expanded Polystyrene Insulation, |
| ETICS | External Thermal Insulation Composite System, |
| FVM | Finite Volume Method, |
| RBF | Radial Basis Functions, |
| SST | Shear-Stress Transport. |

## References

1. Zheng, H.; Gao, G.; Zhong, X.; Zhao, L. Monitoring and Diagnostics of Buildings' Heat Loss Based on 3D IR Model of Multiple Buildings. *Energy Build.* **2022**, *259*, 111889. [CrossRef]
2. Gong, Q.; Kou, F.; Sun, X.; Zou, Y.; Mo, J.; Wang, X. Towards Zero Energy Buildings: A Novel Passive Solar House Integrated with Flat Gravity-Assisted Heat Pipes. *Appl. Energy* **2022**, *306*, 117981. [CrossRef]
3. Chen, J.; Wang, H.; Xie, P.; Najm, H. Analysis of Thermal Conductivity of Porous Concrete Using Laboratory Measurements and Microstructure Models. *Constr. Build. Mater.* **2019**, *218*, 90–98. [CrossRef]
4. Park, H.M.; Lee, J.H.; Kim, K.D. Wall Temperature Prediction at Critical Heat Flux Using a Machine Learning Model. *Ann. Nucl. Energy* **2020**, *141*, 107334. [CrossRef]
5. Xue, X.; Han, S.; Guo, D.; Zhao, Z.; Zhou, B.; Li, F. Study of the Convective Heat Transfer Coefficient of Different Building Envelope Exterior Surfaces. *Buildings* **2022**, *12*, 860. [CrossRef]
6. Clarke, J.A. *Energy Simulation in Building Design*, 2nd ed.; Butterworth-Heinemann: Oxford, UK, 2001; ISBN 0750650826.
7. Thomas, T.R.; Probert, S.D. Thermal Contact Resistance: The Directional Effect and Other Problems. *Int. J. Heat Mass Transf.* **1970**, *13*, 789–807. [CrossRef]
8. Yüncü, H. Thermal Contact Conductance of Nominaly Flat Surfaces. *Heat Mass Transf.* **2006**, *43*, 1–5. [CrossRef]
9. Defraeye, T.; Blocken, B.; Carmeliet, J. Convective Heat Transfer Coefficients for Exterior Building Surfaces: Existing Correlations and CFD Modelling. *Energy Convers. Manag.* **2011**, *52*, 512–522. [CrossRef]
10. Wodołażski, A.; Howaniec, N.; Jura, B.; Bąk, A.; Smoliński, A. Cfd Numerical Modelling of a Pv–Teg Hybrid System Cooled by Air Heat Sink Coupled with a Single-Phase Inverter. *Materials* **2021**, *14*, 5800. [CrossRef]
11. Zeng, H.; Lu, C.; Zhang, L.; Yang, T.; Jin, M.; Ma, Y.; Liu, J. Prediction of Temperature Distribution in Concrete under Variable Environmental Factors through a Three-Dimensional Heat Transfer Model. *Materials* **2022**, *15*, 1510. [CrossRef]
12. Morris Grenfell, D. Heat Transfer by Radiation. In *Building Heat Transfer*; Routledge: Abingdon, UK, 2004; pp. 115–148, ISBN 9780470020555.
13. Rohsenow, W.M.; Hartnett, J.P.; Cho, Y.I. (Eds.) *Handbook of Heat Transfer*, 1st ed.; McGraw-Hill Education: New York, NY, USA, 1998; ISBN 9780070535558.
14. Oosthuizen, P.H.; Naylor, D. Heat Transfer Through a Double-Glazed Window. In *Heat-Transfer Calculations*; Kutz, M., Ed.; McGraw-Hill Education: New York, NY, USA, 2006; ISBN 9780071410410.
15. Ohlsson, K.E.A.; Östin, R.; Grundberg, S.; Olofsson, T. Dynamic Model for Measurement of Convective Heat Transfer Coefficient at External Building Surfaces. *J. Build. Eng.* **2016**, *7*, 239–245. [CrossRef]

16. Barnat-Hunek, D.; Grzegorczyk-Frańczak, M.; Suchorab, Z. Surface Hydrophobisation of Mortars with Waste Aggregate by Nanopolymer Trietoxi-Isobutyl-Silane and Methyl Silicon Resin. *Constr. Build. Mater.* **2020**, *264*, 120175. [CrossRef]
17. Jayamaha, S.E.G.; Wijeysundera, N.E.; Chou, S.K. Measurement of the Heat Transfer Coefficient for Walls. *Build. Environ.* **1996**, *31*, 399–407. [CrossRef]
18. Peng, Z.; Carrigan, S.; Kornadt, O. Investigation of the Influence of Different Room Geometries and Wall Thermal Transmittances on the Heat Transfer in Rooms with Floor Heating. *Energy Build.* **2024**, *317*, 114391. [CrossRef]
19. Viegas, C.A.; Borsoi, G.; Moreira, L.M.; Parracha, J.L.; Nunes, L.; Malanho, S.; Veiga, R.; Flores-Colen, I. Diversity and Distribution of Microbial Communities on the Surface of External Thermal Insulation Composite Systems (ETICS) Facades in Residential Buildings. *Int. Biodeterior. Biodegrad.* **2023**, *184*, 105658. [CrossRef]
20. Xu, H.; Wang, H.; Huo, Q.; Qin, Y.; Zhou, H. Comparative Study of Chinese, European and ISO External Thermal Insulation Composite System (ETICS) Standards and Technical Recommendations. *J. Build. Eng.* **2023**, *68*, 105687. [CrossRef]
21. Directive (EU) 2024/1275 of the European Parliament and of the Council of 24 April 2024 on the Energy Performance of Buildings; 2024; p. 68. Available online: https://eur-lex.europa.eu/eli/dir/2024/1275 (accessed on 1 July 2024).
22. Saber, H.H.; Yarbrough, D.W. Advanced Modeling of Enclosed Airspaces to Determine Thermal Resistance for Building Applications. *Energies* **2021**, *14*, 7772. [CrossRef]
23. Orlik-Kożdoń, B. Polystyrene Waste in Panels for Thermal Retrofitting of Historical Buildings: Experimental Study. *Energies* **2021**, *14*, 1844. [CrossRef]
24. Golder, S.; Narayanan, R.; Hossain, M.R.; Islam, M.R. Experimental and CFD Investigation on the Application for Aerogel Insulation in Buildings. *Energies* **2021**, *14*, 3310. [CrossRef]
25. Rehman, A.U.; Sheikh, S.R.; Kausar, Z.; McCormack, S.J. Numerical Simulation of a Novel Dual Layered Phase Change Material Brick Wall for Human Comfort in Hot and Cold Climatic Conditions. *Energies* **2021**, *14*, 4032. [CrossRef]
26. Basok, B.; Pavlenko, A.; Novikov, V.; Koshlak, H.; Ciosek, A.; Moroz, M. Comprehensive Investigation of the Thermal Performance of an Electrically Heated Double-Glazed Window: A Theoretical and Experimental Approach. *Energies* **2024**, *17*, 4491. [CrossRef]
27. Alaidroos, A. Transient Behavior Analysis of the Infiltration Heat Recovery of Exterior Building Walls. *Energies* **2023**, *16*, 7198. [CrossRef]
28. Urzędowski, A.; Zaburko, J.; Gleń, P.; Łagód, G. Numerical and Experimental Investigation of the Influence of External Wall Moisture on Building Temperature Distributions. *Adv. Sci. Technol. Res. J.* **2021**, *15*, 297–308. [CrossRef]
29. Makaveckas, T.; Bliūdžius, R.; Burlingis, A. The Influence of Different Facings of Polyisocyanurate Boards on Heat Transfer Through the Wall Corners of Insulated Buildings. *Energies* **2020**, *13*, 1991. [CrossRef]
30. Babiarz, B.; Krawczyk, D.A.; Siuta-Olcha, A.; Manuel, C.D.; Jaworski, A.; Barnat, E.; Cholewa, T.; Sadowska, B.; Bocian, M.; Gnieciak, M.; et al. Energy Efficiency in Buildings: Toward Climate Neutrality. *Energies* **2024**, *17*, 4680. [CrossRef]
31. Fan, C.; Xia, X.L.; Du, W.; Sun, C.; Li, Y. Numerical Investigations of the Coupled Conductive-Radiative Heat Transfer in Alumina Ceramics. *Int. Commun. Heat Mass Transf.* **2022**, *135*, 106097. [CrossRef]
32. Urzędowski, A.; Styczeń, J.; Wójcicka-Migasiuk, D. Analysis of thermal properties and heat loss in construction and isothermal materials of multilayer building walls. *Adv. Sci. Technol. Res. J.* **2017**, *11*, 33–37. [CrossRef]
33. Kats, D.; Wang, Z.; Gan, Z.; Liu, W.K.; Wagner, G.J.; Lian, Y. A Physics-Informed Machine Learning Method for Predicting Grain Structure Characteristics in Directed Energy Deposition. *Comput. Mater. Sci.* **2022**, *202*, 110958. [CrossRef]
34. Chen, L.; Zhang, Y.; Zhou, X.; Shi, X.; Yang, L.; Jin, X. A New Method for Measuring Thermal Resistance of Building Walls and Analyses of Influencing Factors. *Constr. Build. Mater.* **2023**, *385*, 131438. [CrossRef]
35. Gonçalves, M.; Simões, N.; Serra, C.; Almeida, J.; Flores-Colen, I.; Vieira de Castro, N.; Duarte, L. Onsite Monitoring of ETICS Comparing Different Exposure Conditions and Insulation Materials. *J. Build. Eng.* **2021**, *42*, 103067. [CrossRef]
36. Agababov, S.G. Effect of the Roughness Factor on Radiation Properties of Solids. *Teplofiz. Vysok. Temp.* **1970**, *8*, 770–773.
37. Zhang, Z.; Chen, M.; Yu, P.; Huang, H.; Li, H.; Yu, F.; Zhang, Z.; Niu, Y.; Gao, S.; Wang, C.; et al. Study of the Roughness Effect on the Normal Spectral Emissivity of GH3044. *Infrared Phys. Technol.* **2023**, *133*, 104831. [CrossRef]
38. Tomkiewicz, D.; Cudzewicz, A.; Górecka-Orzechowska, J. Zastosowanie Programu FLUENT Do Modelowania Zjawisk Termodynamicznych w Komorze Klimatycznej. *Inżynieria Rol.* **2011**, *15*, 239–245.
39. Sachajdak, A.; Słoma, J.; Szczygieł, I. Thermal Model of the Gas Metal Arc Welding Hardfacing Process. *Appl. Therm. Eng.* **2018**, *141*, 378–385. [CrossRef]
40. Korkerd, K.; Zhou, Z.; Zou, R.; Piumsomboon, P.; Chalermsinsuwan, B. Effect of Immersed Tubes Configurations on Mixing and Heat Transfer of Mixed Biomass and Silica Sand in a Bubbling Fluidized Bed Using CFD-DEM and Statistical Experimental Design Analysis. *Powder Technol.* **2024**, *437*, 119542. [CrossRef]
41. Jamińska-Gadomska, P.; Lipecki, T.; Pieńko, M.; Podgórski, J. Wind Velocity Changes Along the Passage Between Two Angled Walls—CFD Simulations and Full-Scale Measurements. *Build. Environ.* **2019**, *157*, 391–401. [CrossRef]
42. Słoma, J.; Szczygieł, I.; Sachajdak, A. Modelling of Thermal Phenomena in Electric Arc During Surfacing. *Arch. Civ. Mech. Eng.* **2011**, *11*, 437–449. [CrossRef]

43. Sachajdak, A.; Lappalainen, J.; Mikkonen, H. Dynamic Simulation in Development of Contemporary Energy Systems—Oxy Combustion Case Study. *Energy* **2019**, *181*, 964–973. [CrossRef]
44. Hoang, M.L.; Verboven, P.; De Baerdemaeker, J.; Nicolaï, B.M. Analysis of the Air Flow in a Cold Store by Means of Computational Fluid Dynamics. *Int. J. Refrig.* **2000**, *23*, 127–140. [CrossRef]
45. Kaleta, A.; Górnicki, K.; Peroń, S.; Szwast, Z.; Kiryjow, J. *Podstawy Techniki Cieplnej w Inżynierii Rolniczej*; Wyd. 2.; Wydawnictwo SGGW: Warsaw, Poland, 2015; ISBN 9788375831054.
46. Norton, T.; Sun, D.W.; Grant, J.; Fallon, R.; Dodd, V. Applications of Computational Fluid Dynamics (CFD) in the Modelling and Design of Ventilation Systems in the Agricultural Industry: A Review. *Bioresour. Technol.* **2007**, *98*, 2386–2414. [CrossRef]
47. Syta, A.; Czarnigowski, J.; Jakliński, P. Detection of Cylinder Misfire in an Aircraft Engine Using Linear and Non-Linear Signal Analysis. *Measurement* **2021**, *174*, 108982. [CrossRef]
48. Jedliński, Ł.; Syta, A.; Gajewski, J.; Jonak, J. Nonlinear Analysis of Cylindrical Gear Dynamics Under Varying Tooth Breakage. *Measurement* **2022**, *190*, 110721. [CrossRef]
49. Barnat-Hunek, D.; Lagod, G.; Klimek, B. Evaluation of the Contact Angle and Frost Resistance of Hydrophobised Heat-Insulating Mortars with Polystyrene. *AIP Conf. Proc.* **2017**, *1866*, 040004.
50. Thongsuk, S.; Songsukthawan, P.; Lertwanitrot, P.; Ananwattanaporn, S.; Yoomak, S.; Pothisarn, C. Impact of Building Envelope Materials on Energy Usage and Performance of Evaporative Cooling System in Residential Building. *Energies* **2024**, *17*, 3748. [CrossRef]
51. Schabowicz, K.; Wójcicka-Migasiuk, D.; Urzędowski, A.; Wróblewski, K. Nondestructive Investigations of Expansion Gap Concrete Roughness. *Measurement* **2021**, *182*, 109603. [CrossRef]
52. Sánchez-Calderón, I.; Merillas, B.; Bernardo, V.; Rodríguez-Pérez, M.Á. Methodology for Measuring the Thermal Conductivity of Insulating Samples with Small Dimensions by Heat Flow Meter Technique. *J. Therm. Anal. Calorim.* **2022**, *147*, 12523–12533. [CrossRef]
53. Urzędowski, A.; Wójcicka-Migasiuk, D.; Buraczyńska, B. Visual Effects of Surface Emissivity in Thermal Imaging. *Adv. Sci. Technol. Res. J.* **2020**, *14*, 215–222. [CrossRef]
54. Nowak, H. The Influence of Environmental Thermal Radiation on the Results of Thermographic Investigation of Buildings. *Bud. Arch.* **2013**, *12*, 059–066. [CrossRef]
55. Shu, S.; Wu, T.; Wang, Z.; Zhang, Y.; Yang, Z.; Liang, H. Research on the Normal Emissivity of Graphite between 150 and 500 °C by an Infrared Camera for Nuclear Fusion Devices. *Nucl. Mater. Energy* **2022**, *31*, 101182. [CrossRef]
56. Węgrzyński, W.; Vigne, G. Experimental and Numerical Evaluation of the Influence of the Soot Yield on the Visibility in Smoke in CFD Analysis. *Fire Saf. J.* **2017**, *91*, 389–398. [CrossRef]
57. Steiner, T.R. High Temperature Steady-State Experiment for Computational Radiative Heat Transfer Validation Using COMSOL and ANSYS. *Results Eng.* **2022**, *13*, 100354. [CrossRef]
58. Sohrabi, N.; Hammoodi, K.A.; Hammoud, A.; Jasim, D.J.; Hashemi Karouei, S.H.; Kheyri, J.; Nabi, H. Using Different Geometries on the Amount of Heat Transfer in a Shell and Tube Heat Exchanger Using the Finite Volume Method. *Case Stud. Therm. Eng.* **2024**, *55*, 104037. [CrossRef]
59. Menter, F.; Kuntz, M.; Langtry, R.B. Ten Years of Industrial Experience with the SST Turbulence Model. *Heat Mass Transf.* **2003**, *4*, 625–632.
60. Menter, F. Two Equation Eddy-Viscosity Turbulence Modeling for Engineering Applications. *AIAA J.* **1994**, *32*, 1598–1605. [CrossRef]
61. Pogorzelski, J.A. Ostrożnie z Niestacjonarnymi Badaniami Przewodności Cieplnej. *Pr. Inst. Tech. Bud.* **2000**, *113*, 38–52.
62. Gawin, D.; Klemm, P.; Konca, P.; Więckowska, A.; Woźniak, J. *Komputerowa Fizyka Budowli: Komputerowa Symulacja Procesów Wymiany Masy i Energii w Budynku: Przykłady Zastosowań*; Wydawnictwo Politechniki Łódzkiej: Łódź, Poland, 1998; ISBN 8387198412.
63. Siegel, A.F.; Wagner, M.R. Chapter 15—ANOVA: Testing for Differences Among Many Samples and Much More. In *Practical Business Statistics*, 8th ed.; Siegel, A.F., Wagner, M.R., Eds.; Academic Press: Cambridge, MA, USA, 2022; pp. 485–510, ISBN 978-0-12-820025-4.
64. Saini, M.C.; Jakhar, O.P. CFD Simulation and Experimental Validation of PCM Thermal Energy Storage System for Micro Trigeneration System Application. *Int. J. Refrig.* **2023**, *149*, 119–134. [CrossRef]
65. Modest, M.F. *Radiative Heat Transfer*; Academic Press Inc.: Cambridge, MA, USA, 2003; ISBN 9780080515632.
66. Andrzejuk, W.; Grzegorczyk-Frańczak, M.; Barnat-Hunek, D.; Franus, M.; Łagód, G. Microstructure, Durability and Surface Free Energy of Lightweight Aggregate Modification of Sanitary Ceramic Wastes and Sewage Sludge. *J. Build. Eng.* **2024**, *93*, 109725. [CrossRef]

67. Chen, J.; Chu, R.; Wang, H.; Xie, P. Experimental Measurement and Microstructure-Based Simulation of Thermal Conductivity of Unbound Aggregates. *Constr. Build. Mater.* **2018**, *189*, 8–18. [CrossRef]
68. Deconinck, L.; Bernardo Quejido, E.; Villa Vidaller, M.T.; Jägle, E.A.; Verbeken, K.; Depover, T. The Mechanism behind the Effect of Building Orientation and Surface Roughness on Hydrogen Embrittlement of Laser Powder Bed Fused Ti-6Al-4V. *Addit. Manuf.* **2023**, *72*, 103613. [CrossRef]